

In Situ Study of the Wet Chemical Etching of SiO₂ and Nanoparticle@SiO₂ Core–Shell Nanospheres

Albert Grau-Carbonell, Sina Sadighikia, Tom A. J. Welling, Relinde J. A. van Dijk-Moes, Ramakrishna Kotni, Maarten Bransen, Alfons van Blaaderen,* and Marijn A. van Huis*



Cite This: *ACS Appl. Nano Mater.* 2021, 4, 1136–1148



Read Online

ACCESS |



Metrics & More

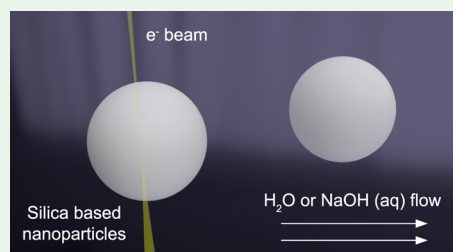


Article Recommendations



Supporting Information

ABSTRACT: The recent development of liquid cell (scanning) transmission electron microscopy (LC-(S)TEM) has opened the unique possibility of studying the chemical behavior of nanomaterials down to the nanoscale in a liquid environment. Here, we show that the chemically induced etching of three different types of silica-based silica nanoparticles can be reliably studied at the single particle level using LC-(S)TEM with a negligible effect of the electron beam, and we demonstrate this method by successfully monitoring the formation of silica-based heterogeneous yolk–shell nanostructures. By scrutinizing the influence of electron beam irradiation, we show that the cumulative electron dose on the imaging area plays a crucial role in the observed damage and needs to be considered during experimental design. Monte-Carlo simulations of the electron trajectories during LC-(S)TEM experiments allowed us to relate the cumulative electron dose to the deposited energy on the particles, which was found to significantly alter the silica network under imaging conditions of nanoparticles. We used these optimized LC-(S)TEM imaging conditions to systematically characterize the wet etching of silica and metal(oxide)–silica core–shell nanoparticles with cores of gold and iron oxide, which are representative of many other core–silica–shell systems. The LC-(S)TEM method reliably reproduced the etching patterns of Stöber, water-in-oil reverse microemulsion (WORM), and amino acid-catalyzed silica particles that were reported before in the literature. Furthermore, we directly visualized the formation of yolk–shell structures from the wet etching of Au@Stöber silica and Fe₃O₄@WORM silica core–shell nanospheres.



KEYWORDS: liquid cell electron microscopy, wet chemical etching, silica nanoparticles, imaging conditions, low dose imaging

1. INTRODUCTION

Silica nanoparticles or core–shell silica–shell nanoparticles are of general interest, as they are biocompatible and stable in a large number of solvents,¹ in which they also form stable dispersed colloidal systems with interactions tunable over a large range of distances.^{2–5} Three widely used strategies to synthesize spherical colloidal silica systems and perform seeded growth of nanoparticles are the Stöber,^{6–8} water-in-oil reverse microemulsion (WORM),^{9–12} and amino acid-catalyzed (AAC) methods^{13–19} (Figure 1A). These approaches all have in common that a basic environment is created in which both the hydrolysis and condensation of tetra- and/or tri-alkoxysilanes are catalyzed by OH[−] ions (Figure 1B). The Stöber method relies on the hydrolysis and condensation of the precursor tetraethyl orthosilicate (TEOS) homogeneously dissolved in an alcoholic aqueous solution while ammonia catalyzes the hydrolysis and condensation reactions.^{6–8} The WORM method also exploits ammonia as the catalyzing agent, but TEOS condensation happens inside the water phase of a water-in-oil microemulsion.^{9–12,20} In the AAC method, TEOS condensation is catalyzed by a basic amino acid (L-lysine, L-arginine) in an aqueous solution.^{14,21} All three synthesis approaches result in spherical, relatively monodisperse particles

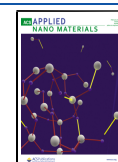
but with potentially different internal silica structures which have shown to be not homogeneous in all cases.^{16,17,22}

The growth mechanism of Stöber silica consists of an initial aggregation process of several nm-sized siloxane moieties, followed by their continuous growth by monomer addition into smoother, spherical particles.^{6–8} The overall growth rate is limited by the speed of the hydrolysis of TEOS, which is the first order reaction. Toward the end of the reaction, the concentration of hydrolyzed silanol groups goes down, the development of siloxane bonds becomes slower, and silicon atoms can form more siloxane bonds (highly condensed silica).^{23,24} This growth mechanism results in an inhomogeneous internal distribution of silica condensation levels.^{16,17,24} WORM silica nanoparticles are also believed to have a less condensed internal structure,²² as the growth conditions are similar to the Stöber method.²⁵ In the AAC method, particles

Received: October 16, 2020

Accepted: December 22, 2020

Published: January 5, 2021



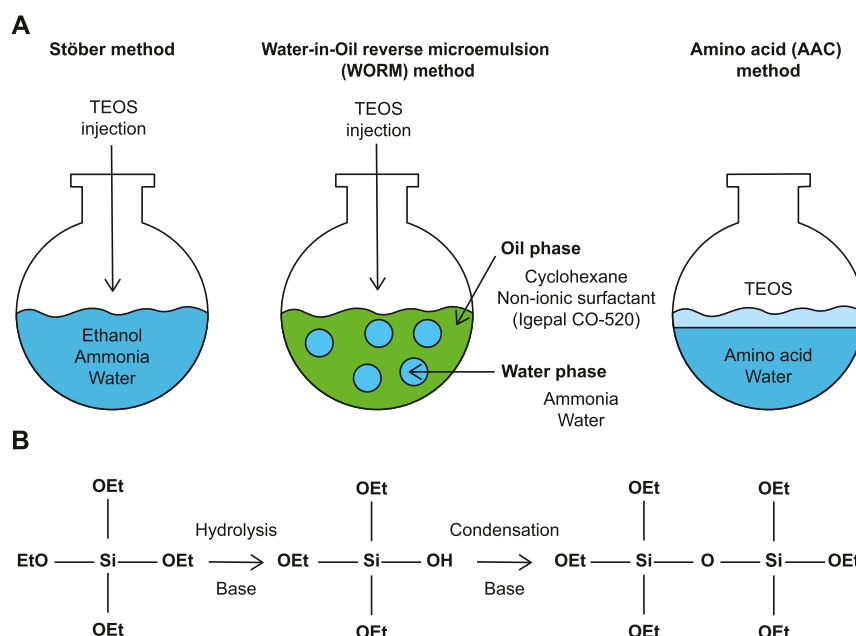


Figure 1. Silica synthesis methods and chemistry. (A) Schematics of the Stöber, AAC and WORM methods to synthesize silica nanospheres. In the Stöber method, silica growth happens in a basic alcoholic solution after the injection of TEOS. In the WORM method, silica growth takes place by the diffusion of TEOS from the oil phase into the basic water droplets of a water-in-oil reverse microemulsion. In the AAC method, silica growth takes place in an aqueous phase containing a basic amino acid from the slow diffusion of hydrolyzed TEOS from an unmixed, oil-like layer of nonhydrolyzed TEOS. (B) TEOS hydrolysis and condensation are two basic steps in silica growth for the Stöber, AAC, and WORM silica nucleation and growth processes. Basic media catalyzes both the condensation and hydrolysis steps. In fully condensed silica, each TEOS molecule has formed four siloxane bonds; however, all these procedures do not produce fully condensed silica.

form in an aqueous environment, typically at relatively elevated temperatures, but less is known of their internal structure.

Understanding the internal distribution of condensation levels in silica particles can help explain the reported differences in properties and behavior, such as the dissolution behaviors of the different types of silica nanospheres.¹³ Silica is slightly soluble at room temperature in pH neutral water,²⁶ and its solubility is strongly dependent on the pH: increased pH values lead to increased solubility.²⁷ When exposed to an etching solution, loosely condensed parts will dissolve more easily than highly condensed parts, as fewer siloxane bonds need to be broken.²³ Therefore, the organization of the condensation degrees of the silica network can be revealed by exposing the nanoparticles to a basic aqueous solution and studying the etching process. Previously, monitoring how the morphology of particles changes in etching studies consisted of several time-consuming cleaning steps in which the etching needed to be quenched and the particles had to be dried for regular (S)TEM analysis. If drying is not done by, for example, critical drying, the drying forces can significantly alter the structures under observation.

Liquid cell (scanning) transmission electron microscopy (LC-(S)TEM) allows *in situ* monitoring of the morphology evolution of nanostructures in chemically active, wet environments^{28–33} and thus could possibly be used to characterize the evolution of silica-based nanoparticles in basic aqueous solutions. LC-(S)TEM studies rely upon the illumination of a sample in a liquid environment by a highly energetic electron beam. However, beyond particular thresholds of intensity, electron beam irradiation is known to directly generate conditions for which particles are affected by radiolysis of the liquid.^{34,35} Until now, the influence of electron irradiation on chemical reactions has been studied extensively for the

stability of precursors in solution^{36–41} but its effects on other chemical processes remain not that well investigated. Wet etching (or dissolution) of nanostructures in LC-(S)TEM has been reported in previous studies, but the effects of electron dosage were only partially evaluated or only evaluated after the sample was exposed to electron beam irradiation.^{28,30} The total dose received by a sample is also known to play an important role on the behavior of systems and the interpretation of LC-(S)TEM results, as the effects of the electron beam accumulate in the damage done.^{37,42} Therefore, describing and understanding the impact of the electron beam exposure on nanoparticles dispersed in chemically reacting solvents is important for the future development of the *in situ* LC-(S)TEM methodology with a particular aim on finding the conditions where these effects can be neglected.

In this study, we first describe the etching of AAC silica particles dispersed in basic aqueous solutions. AAC silica nanoparticles, contrary to Stöber and WORM-type silica nanoparticles, were found to reduce in size continuously from the outside inward. Next, we made use of this better-defined etching of AAC silica nanoparticles to characterize the effects of the electron beam irradiation on this type of silica particles immersed in water and in basic aqueous solutions. The cumulative electron dose during the LC-(S)TEM imaging of the wet etching of silica nanoparticles was the main parameter regarding electron beam effects. Our findings revealed that the effects of the electron beam on the etching and stability of silica nanoparticles can be reduced and even made negligible by minimizing the cumulative electron dose on the particles, independent of the electron dose rate. Furthermore, we found that the electron irradiation directly affected the wet chemical etching of silica by depositing enough energy in the silica to severely alter the siloxane

network. This knowledge was used to characterize the wet etching of Stöber and WORM silica nanoparticles and $\text{Fe}_3\text{O}_4@$ WORM silica and $\text{Au}@$ Stöber silica core-shell nanoparticles. The inhomogeneous etching patterns of silica-based nanospheres synthesized *via* different methods were characterized. We report the direct imaging of the void formation step of yolk-shell nanoparticles from metal(oxide)*@*silica core-shell nanospheres *via* the inhomogeneous etching of the silica shell. LC-(S)TEM shows that the core became mobile during this void formation. Describing the behavior of the gold and iron oxide core-shell silica particles, which are representative of NP*@*silica core-shell systems in general, during the yolk-shell formation can lead to a better understanding of the final product, and potentially open the door to new synthesis procedures.

2. EXPERIMENTAL METHODS

2.1. Materials. The following chemicals were used: TEOS (99%, Sigma-Aldrich), L-arginine (98%, Sigma-Aldrich), absolute ethanol (Merck), MilliQ water (Millipore system), sodium hydroxide (reagent grade, $\geq 98\%$, pellets, Sigma-Aldrich), hydrogen tetrachloroaurate trihydrate ($\text{HAuCl}_4 \cdot 3\text{H}_2\text{O}$, $\geq 99.9\%$, Sigma-Aldrich), sodium citrate tribasic dihydrate ($\geq 99.0\%$, Sigma-Aldrich), polyvinylpyrrolidone (PVP, 10000 g/mol), polyoxyethylene (5) nonylphenyl ether (IGEPAL CO-520, Sigma-Aldrich), ammonia (NH_3 , 30 wt %, Sigma-Aldrich), iron chloride ($\text{FeCl}_3 \cdot 6\text{H}_2\text{O}$, 98%, Sigma-Aldrich), sodium oleate (95%, TCL), hexane (98%, Sigma-Aldrich), oleic acid (90%, Sigma-Aldrich), 1-octadecene (90%, Sigma-Aldrich), and potassium persulfate ($\text{K}_2\text{S}_2\text{O}_8$, $\geq 99\%$, Sigma-Aldrich).

2.2. Synthesis Protocols. **2.2.1. Stöber Silica Spheres.** Stöber silica particles (120 nm, PD: 11%) were synthesized with a simple one pot synthesis. A 1000 mL round bottom flask was cleaned thoroughly with ethanol and milliQ water. Then, 500 mL of absolute ethanol was added. 33.3 mL of ammonia was added, and the flask was stirred at 600 rpm. Then, 20 mL (90 mmol) of TEOS was injected on the top of the stirring cone. The flask was sealed and stirred overnight. The particles were cleaned by centrifugation steps with ethanol and milliQ water.

2.2.2. AAC Silica Spheres. AAC silica particles (113 nm diameter, PD: 3%) were synthesized with a three step synthesis based on previous literature.⁴³ All glassworks were etched of residual silica of former silica synthesis *via* a base bath (2–3 days in a saturated solution of KOH in ethanol, rinsed with milliQ water). First, 28 nm cores were synthesized as follows: in a 500 mL 1-neck flask, 182.5 mg (6 mM) of L-arginine was dissolved in 169 mL of milliQ water. The mixture was heated to 70 °C and stirred slowly (200 rpm). After 1 h, 11.2 mL (49 mmol) of TEOS was added slowly *via* the wall. The reaction mixture was stirred for 1 day to complete the synthesis. These cores were overgrown up to a diameter of 55 nm as follows: in a 500 mL 1-neck flask (base bath, KOH in ethanol), 183.5 mg (6 mM) of L-arginine was dissolved in 169 mL of milliQ water. 19.3 mL of the dispersion of 28 nm silica particles was added. The mixture was heated to 70 °C and stirred slowly (200 rpm). After 1 h, 11.2 mL (49 mmol) of TEOS was added slowly *via* the wall. The reaction mixture was stirred for 1 day to complete the synthesis. These nanoparticles were overgrown up to the final 113 nm diameter as follows: in a 500 mL 1-neck flask (base bath, KOH in ethanol), 182 mg (0.006 M) of L-arginine was dissolved in 169 mL of milliQ water. 19.3 mL of the dispersion of 55 nm silica particles was added. The mixture was heated to 70 °C and stirred slowly (200 rpm). After 1 h, 11.2 mL (49 mmol) of TEOS was added slowly *via* the wall. The reaction mixture was stirred for 1 day to complete the synthesis. If desired, the final size of AAC spheres could be tuned by tuning the initial volume of TEOS (Figure S1).

2.2.3. WORM Silica Spheres. WORM silica spheres (30 nm diameter) were synthesized following the WORM method.^{44,45} 20 mL of cyclohexane and 1.6 mL of IGEPAL CO-520 were mixed and stirred for 15 min. To this solution, 120 μL of NH_4OH solution and 30 μL of

milliQ water were added. After 15 min, 360 μL (2 mmol) of TEOS was added, and the reaction mixture was left under stirring for 12 h at room temperature. The resultant colloids were centrifuged (7500g, 15 min) and washed with absolute ethanol. The solid product was then redispersed in ethanol.

2.2.4. Au@Stöber Silica Core-Shell Spheres. Citrate-stabilized spherical AuNPs (15.5 nm diameter) were synthesized using the sodium citrate reduction method.^{1,3} 200 mL of H_2O and 2.0 mL of an aqueous solution containing 10 g/L $\text{HAuCl}_4 \cdot 3\text{H}_2\text{O}$ were added to a 500 mL two-neck flask with a stirring bar and reflux condenser. The flask was placed in an oil bath and heated until boiling. Then, 6.0 mL of an aqueous solution containing 10 g/L sodium citrate tribasic dihydrate was rapidly added under vigorous stirring (1200 rpm), and the mixture was left refluxing and stirring for 15 min during which a color change from yellow to dark blue to pink and finally deep red was observed. The stirring was slowed down to 400 rpm, and the mixture was allowed to cool down to room temperature. Au@Stöber NPs were synthesized as follows: 2.4 mL of 10 wt % PVP⁵ in water was added to 100 mL of the as-synthesized AuNPs and stirred (300 rpm) for 24 h. The PVP-coated particles were collected by means of centrifugation (15000g, 1 h.), redispersed in 100 mL of ethanol, and added to a 300 mL Erlenmeyer flask. Then, 10 mL of ammonium hydroxide solution was added, followed by 0.2 mL of 10% (V/V) TEOS in ethanol solution under vigorous stirring (1200 rpm) and was left stirring. After 90 min, another 0.4 mL of 10% TEOS in ethanol solution was added and left to react for 90 min after which the particles were collected using centrifugation (15000g, 1 h), redispersed in ethanol, centrifuged, and finally redispersed in 10 mL of ethanol. The ethanolic particle dispersion was stored at room temperature for at least 1 year without loss of colloidal stability.

2.2.5. Magnetite (Fe_3O_4)@WORM Silica Core-shell Spheres. Monodisperse magnetite nanoparticles (9 nm diameter) were prepared from an iron oleate precursor by thermal decomposition as described in the literature.⁴⁶ The method involves two steps. In the first step, the metal-oleate precursor was synthesized by reacting iron chloride ($\text{FeCl}_3 \cdot 6\text{H}_2\text{O}$) with sodium oleate. In the second step, this metal-oleate precursor was further heated to 320 °C using the high boiling point solvent 1-octadecene. The solution was kept at this temperature for 30 min, which led to the nucleation and growth of the nanoparticles. The resulting solution was washed with excess acetone and collected by centrifugation and dispersed in hexane or cyclohexane. To synthesize the core-shell magnetite-silica spheres (40 nm diameter), we followed the WORM method.^{11,44,45} In a typical synthesis procedure, 2.5 mg of Fe_3O_4 nanoparticles stabilized by oleic acid as ligands was dispersed in 20 mL of cyclohexane and 1.6 mL of IGEPAL CO-520 and was stirred for 15 min. To this solution, 120 μL of NH_4OH solution and 30 μL of milliQ water were added. After 15 min, 360 μL (2 mmol) of TEOS was added and the reaction mixture was left under stirring for 12 h at room temperature. The resultant colloids were centrifuged and washed with absolute ethanol. The solid product was then dispersed in ethanol.

2.3. Ex situ Etching Experiments. Nanoparticles were dispersed in plastic vials with final concentrations of 0.6 $\text{mg}\cdot\text{mL}^{-1}$ (10 mM) in NaOH aqueous solutions with the desired base concentrations and were left to react for the desired amount of time. Samples were collected by drop-casting on Formvar/Carbon Film 200 Mesh Copper TEM grids after one cleaning step consisting of 10 min of centrifugation at 20000g and redispersion in milliQ water.

2.4. In situ Liquid Cell Experiments. Experiments were performed using a liquid cell dedicated holder [Hummingbird Scientific, (USA)]. Heating LC-(S)TEM experiments were performed using a liquid cell dedicated holder with heating capabilities [Protochips, (USA)]. Silicon chips with silicon nitride (SiN) windows (50 \times 200 μm , 50 nm thickness) were used to encapsulate the liquid volume. In all experiments, spacers of 100 or 250 nm were used. The side of the chips which were in contact with liquid were glow-discharged for 90 s prior use. Around 2 μL of a diluted suspension (0.06 $\text{mg}\cdot\text{mL}^{-1}$) of the desired nanoparticles was drop-casted on the top chip and let to dry; this way, a number of particles were found to be attached to the top window during the experiments. Then, the

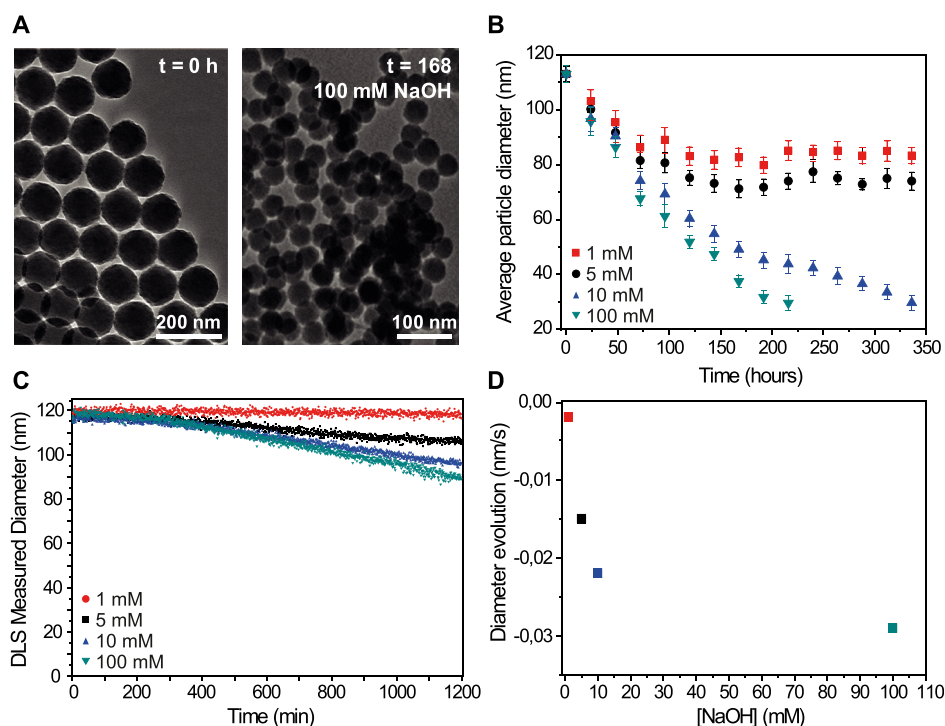


Figure 2. *Ex situ*, bulk etching of AAC silica nanoparticles. (A) TEM imaging of AAC silica particles dried after being dispersed in a NaOH aqueous solution. AAC silica particles etch homogeneously, decreasing in size over time. (B) Time evolution of the etching process of AAC silica spheres in aqueous NaOH solutions. The data was obtained from TEM imaging of dried samples taken at different time points. (C) Time evolution of the etching process of AAC silica spheres in aqueous NaOH solutions followed by DLS during the first 20 h of the process. The etching process shows two parts. For the first hours (up to around 300 min), the decrease in diameter was slow. The second part (from 300 to 1200 min) of the etching process showed a faster decrease of diameter. (D) Slope of the second part of the etching was fitted by linear regression. The speed of the etching increased with the base concentration, but the change in rate was smaller for higher base concentrations. The color of each data point refers to the base concentration as depicted in C.

bottom chip was placed in a dedicated holder; 2 μL of milliQ water was drop-casted on it, and then, the top chip was placed into position aligned over the bottom window. Excess water was removed with filter paper, and the cell was sealed. To allow the flow of solutions into the set-up, a Hamilton syringe pump was utilized with a 1 mL glass syringe. In heating experiments, heating ramps did not exceed 1 $^{\circ}\text{C}/\text{s}$ slopes to avoid bubble formation.

2.5. Sample Characterization and Imaging. **2.5.1. Dynamic Light Scattering.** The *ex situ* etching of AAC silica spheres was followed *via* dynamic light scattering (DLS) with a Zetasizer Nano ZS. A dispersion of AAC silica spheres with a final particle concentration of 0.6 $\text{mg}\cdot\text{mL}^{-1}$ was prepared in an aqueous solution with the desired NaOH concentration. The particle size was measured continuously every 10 s and averaged per minute.

2.5.2. (S)TEM. Imaging at 200 keV was carried out with a Tecnai-F20 (200 keV) transmission electron microscope (TEM, Thermo Fisher Scientific) equipped with a field emission gun. Imaging at 120 keV was carried out with a Talos L120C transmission electron microscope (Thermo Fisher Scientific). Scanning TEM [(S)TEM] imaging was performed with an annular dark-field detector (ADF, E.A. Fischione Instruments Inc., model 3000, USA) at a camera length of 120 mm. In order to calculate the electron dose rate, the beam current in vacuum was measured for each spot size and the resulting electron dose rate was calculated by dividing the beam current by the total frame size as follows⁴⁷

$$d = \frac{I_e}{eA} \quad (1)$$

Here, d is the electron dose rate, I_e is the beam current, e is the elementary charge, and A is the total frame size determined by magnification. Free-hand lithography was performed by manually moving the position of a stationary electron beam with a beam current of 70 pA.

3. RESULTS AND DISCUSSION

3.1. AAC Silica Spheres as the Model System to Study Electron Beam Effects on Wet Silica Etching. To study the effects of the electron beam irradiation on the wet etching of silica nanospheres, a system of nanoparticles with a quantifiable etching pattern was required. Comparing the LC-(S)TEM observations of etching processes with their known *ex situ* counterparts would expose the effects of the electron beam irradiation. Furthermore, a system with low polydispersity would make single particle LC-(S)TEM observations comparable. Also, the nanoparticles should be large enough to allow their study at low magnifications and low electron beam intensities to explore the lower range of electron dose rates. Of all silica systems, AAC silica nanoparticles were chosen because of their low polydispersity and the precise size control from synthesis they offer. We characterized the *ex situ* etching of AAC silica nanoparticles ($d = 113$ nm, PD: 3%, silica concentration: 10 mM) dispersed in NaOH aqueous solutions. We monitored the etching process by taking samples in time to compare the bulk etching with the *in situ* etching inside the liquid cell (Figure 2). AAC silica spheres showed an homogeneous decrease in diameter when exposed to the basic media (Figure 2A). The etching process lasted up to weeks if enough NaOH was present in the system (Figures 2B and S2) and could be used to easily tune the size of a batch of AAC silica spheres to any desired size. The polydispersity of the AAC silica nanoparticles increased as the particle size reduced during etching while the width of the size distribution remained roughly the same (Figure S3). These observations

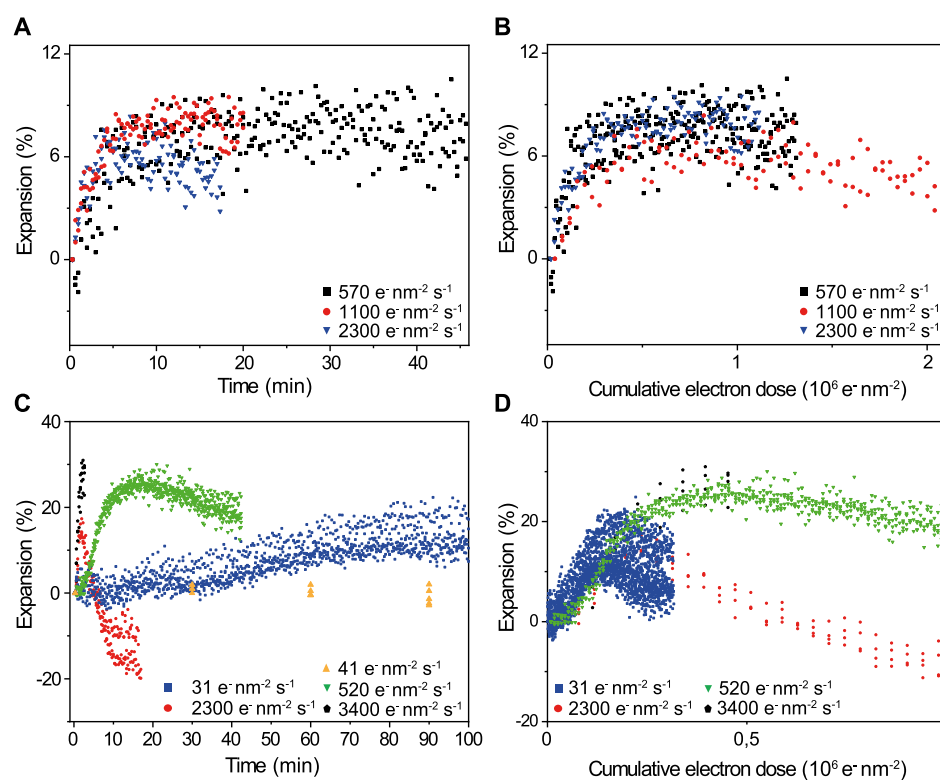


Figure 3. *In situ* etching of AAC silica monitored by liquid cell (S)TEM. (A) Time evolution of the size of AAC spheres in pure water under different electron dose rates. The size evolution of the same experiments as a function of the cumulative electron dose is shown in (B). (C) Time evolution of the size of AAC spheres in a 100 mM NaOH aqueous solution under different electron dose rates. The size evolution of the same experiments as a function of the cumulative dose is shown in (D). Every electron dose rate for each panel contains data of 4 to 5 different nanoparticles. The flow rate was $5 \mu\text{L}\cdot\text{min}^{-1}$ in all experiments.

indicate that AAC silica was not found to etch through a more condensed outer shell as Stöber and WORM-based silica was found to do.^{13,18,19} A similar etching behavior was observed when AAC silica nanoparticles were etched in HF aqueous solutions (Figure S4). Furthermore, the etching of AAC silica particles was much slower than the etching of Stöber and WORM-based silica, as the dissolution of the latter completed overnight. Here, AAC silica particles were synthesized at higher temperatures than the Stöber particles. Silica further condenses when the temperature is increased,¹⁶ but the final AAC silica particles have condensation levels similar to the other types of silica grown at lower temperatures. As amino acids become incorporated inside the silica particles by adsorbing to the nuclei,¹⁷ these aggregating smaller silica units¹⁹ are probably more highly condensed.^{15,19}

The homogeneous internal structure of AAC silica spheres was further studied by closely following their etching in time. As the diameter of the particles changed gradually, DLS was used as a suitable technique to follow their etching in the presence of different NaOH concentrations (Figure 2C). The etching process happened in two different phases. For the first ~ 300 min, the particle size decreased slowly (less than 5 nm in a 100 mM NaOH solution). After this initial regime, the etching rate increased and the particle size showed a more pronounced decrease. This second phase was studied as a linear process to compare the etching rates between various base concentrations. It can be readily observed that as the base concentration increased, the etching rate did increase as well (Figure 2D). However, the positive trend of the etching rate slowed down at higher pH.

3.2. Characterization of the Electron Beam Irradiation Effects on the Stability and the Wet Etching of AAC Silica Particles.

LC-(S)TEM allowed us to study the wet etching of silica nanoparticles at the single particle level by exposing them to an aqueous NaOH solution during (S)TEM imaging. We showed that AAC silica nanoparticles exhibit two different regimes of etching during the first hours of etching. Here, we exploited the mode of etching of the AAC silica colloids during the first hours in a 100 mM NaOH aqueous solution to determine the conditions under which the silica wet etching process would not be altered by the electron beam. The expected behavior was a slow etching of the spheres, and any change in such behavior could be ascribed to electron beam effects. The low degree of polydispersity of the initial AAC silica particles (3%) allowed for the precise analysis of the morphological evolution of the particles. The size evolution of the particles was followed by digital analysis *via* ellipsoid fitting to binarized data sets as it was done before in the literature.³¹ We prepared the liquid cell set-up as described in the methods; the top window of the chip was covered with the nanoparticles. A region of particles was used to focus on the window; then, the imaging area was shifted with the beam blanked to avoid unnecessary irradiation of any area of interest, after which imaging was performed. If the experiment was conducted under NaOH aqueous solution flow, the imaging was started when the liquid leaving the holder outlet was found to be at the desired pH by probing it with pH paper, which was the case one or 2 min after the flow was started. The constant flow of the base ensured that the cell was always under a flow of basic solution and in contact with a constantly renewed

reservoir of the base. Maintaining a flow of basic solution has been shown to prevent base depletion during wet etching of silica in liquid cell experiments.⁴⁸ The use of buffers could also help maintain the pH inside the cell during etching experiments. However, this function is already fulfilled by the constant flow set-up. Furthermore, buffers have been suggested to partially work as stabilizers of silica during STEM imaging in water, but this role would be mainly a result of their radical scavenging ability.³¹ Therefore, to better decouple the beam effects to the radical scavenging effects, we did not use scavengers during our experiments. The influence of radiolysis radicals and radical scavengers will be discussed in later parts of this study.

Continuous imaging was performed with 1024×1024 pixels, $16 \mu\text{s}$ dwell time, and 1.58 or 0.78 nm pixel sizes. The nanoparticles were first imaged while pure water was flowing into the cell (milliQ grade, $5 \mu\text{L}\cdot\text{min}^{-1}$). Our LC-(S)TEM observations showed that in pure water, the particles expanded gradually up to $\sim 10\%$ of their starting size (Figure 3A, Supporting Information Videos 1, 2 and 3) and subsequently dissolved, in agreement with previous LC-(S)TEM studies of silica particles in water at high electron dose rates.³¹ The initial expansion under a flow of pure water happened at a similar rate for all electron dose rates ranging from 570 to $2.3 \times 10^3 \text{ e}^- \text{ nm}^{-2} \text{ s}^{-1}$, but the dissolution was faster for higher electron dose rates. When the behaviors were compared for similar accumulated doses, they became almost the same (Figure 3B). The electron beam irradiation in pure water is known to change the pH of the solution to more acidic values and to produce a number of reducing and oxidizing agents.³⁴ Scavenging some of these radicals [$\text{e}^-(\text{aq})$, H^\bullet] was shown to increase silica stability in water during LC-(S)TEM experiments.³¹

AAC silica spheres were remarkably more affected by the electron beam if the particles were imaged under a flow of a basic aqueous solution (100 mM NaOH (aq) , $5 \mu\text{L}\cdot\text{min}^{-1}$). Pronounced expansion was consistently observed if the system was imaged in 100 mM NaOH aqueous media for all of the used electron dose rates (Figure 3C, Supporting Information Videos 4, 5, 6 and 7). The expansion was found to amount to up to $\sim 30\%$ of the initial size of the nanoparticles. This process was faster for higher electron dose rates, ranging from a few minutes for dose rates of $2.3 \times 10^3 \text{ e}^- \text{ nm}^{-2} \text{ s}^{-1}$ and $3.4 \times 10^3 \text{ e}^- \text{ nm}^{-2} \text{ s}^{-1}$ to around 20 min for a dose rate of $520 \text{ e}^- \text{ nm}^{-2} \text{ s}^{-1}$ to a number of hours for a dose rate of $31 \text{ e}^- \text{ nm}^{-2} \text{ s}^{-1}$. The disparity was completely lost when the expansion was considered as a function of the cumulative dose on the frame (Figure 3D). The onset and initial evolution of all the expansions happened at similar cumulative electron doses, regardless of the electron dose rate. On the other hand, the dissolution process remained different for different dose rates even if these were compared *via* the total accumulated doses. At low dose rates ($31 \text{ e}^- \text{ nm}^{-2} \text{ s}^{-1}$), expansion was slow as few electrons were deposited per frame. This allowed the concurrent dissolution process to take place extensively during the expansion period, and therefore, the overall expansion was not as high as in other cases. Even at such low electron dose rates, the dissolution phase was accelerated by electron beam irradiation as compared to the *ex situ* counterpart experiments. At a moderate electron dose rate ($520 \text{ e}^- \text{ nm}^{-2} \text{ s}^{-1}$), the expansion happened faster, and therefore, the dissolution could not play a large role during the expansion phase. The dissolution of the particles happened faster for higher dose

rates than for lower dose rates as the network was continuously affected by the electron beam irradiation. At a high electron dose rate ($2.3 \times 10^3 \text{ e}^- \text{ nm}^{-2} \text{ s}^{-1}$), the network was so strongly affected by imaging that the dissolution was faster also during particle expansion. This resulted in a slightly reduced expansion but also in much accelerated dissolution. Finally, at an even higher electron dose rate ($3.4 \times 10^3 \text{ e}^- \text{ nm}^{-2} \text{ s}^{-1}$), expansion happened so fast that the dissolution process could not affect the expansion period. At such high electron dose rates, the scanning induced the deformation of silica particles in the scanning direction, as previously reported for silica spheres and colloidal silica rods under intense STEM illumination.^{31,48,49} Although this process is still not well understood, silica plasticity increases under electron irradiation even at room temperature,⁵⁰ and thus, we might be observing the effects of the intense electric fields created by secondary electron ejection from the surfaces in the liquid cell.⁵¹ To summarize, our results indicate that the expansion process of silica particles upon electron beam irradiation in the presence of water appears to be completely driven by the cumulative electron dose rate on the particle and that the extent of such expansion depends on the media in which the particles are immersed in. On the other hand, the dissolution process was not only related to the cumulative electron dose. The different dissolution rates are better understood when considering the direct interaction of the electron beam with the silica network, together with the passive dissolution process taking place between the nanoparticle and the surrounding liquid phase. Accelerated dissolution or “superdissolution” of oxides has been reported for other oxides and linked to the generation of an oxygen deficient surface by the electron beam and the consequent reduction of the activation energy at the surface.^{52,53} As higher electron dose rates result in higher concentrations of radiolysis products, the dissolution phase is then also sensitive to this parameter. The accelerated dissolution of silica under electron irradiation in water has indeed been partially slowed down by the use of radical scavengers in solution, further supporting our findings.³¹ We were also able to perform free-hand lithography on our AAC particles immersed in water, similarly to previous results in CeO thin films (Figure S5).⁵² Low electron dose rates are crucial to minimize electron beam effects on the diffusion motion of nanoparticles⁵⁴ and might become an increasingly important parameter in future experiments. In conclusion, the etching of AAC silica nanoparticles was best imaged by minimizing the electron dose rate and, more importantly, the cumulative electron dose. Considering this, the relative stability of AAC silica particles during the first hours exposed to a 100 mM NaOH aqueous solution was successfully characterized by using a low electron dose rate ($41 \text{ e}^- \text{ nm}^{-2} \text{ s}^{-1}$) and discontinuous imaging (with 30 min blanks) to reduce the amount of electrons accumulated on the imaging area to approximately $2751 \text{ e}^- \text{ nm}^{-2}$ (1024×1024 pixels, $16 \mu\text{s}$ dwell time, 1.58 nm pixel size) (Figure 3C, yellow triangle data, Supporting Information Video 8).

Even though the accelerated dissolution phase of oxides has been already reported and partially studied in the literature, the expansion phase reported here has not been explored much. Therefore, we experimentally probed the mechanism behind the expansion of silica in water and 100 mM NaOH under electron irradiation. First, we assessed the role of water radiolysis radicals in this process. Expansion was more severe for a solution with 100 mM NaOH in comparison to pure

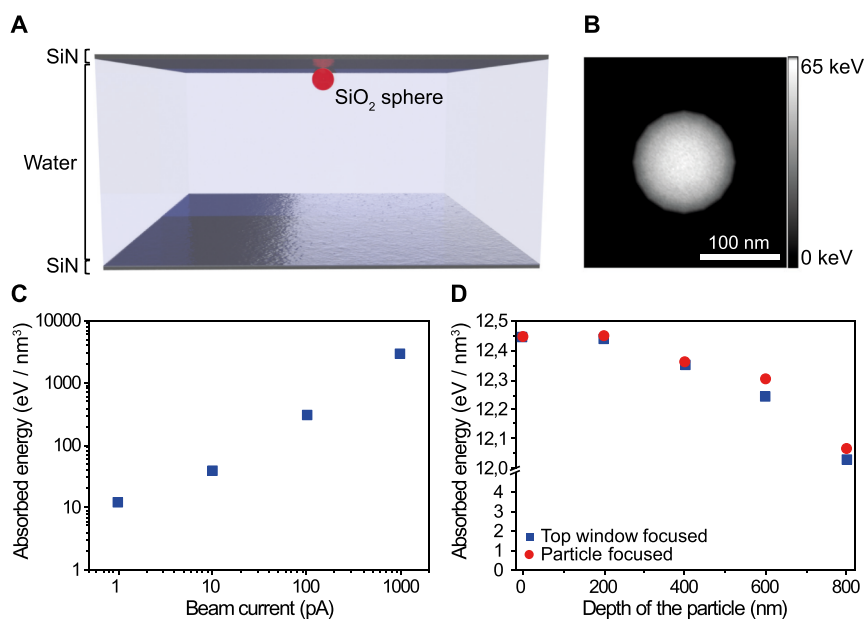


Figure 4. Simulation of pathways of electrons during (S)TEM imaging simulated with the CASINO software package. (A) Schematic of the simulated geometry. A $1 \mu\text{m}$ water layer was placed between 50 nm silicon nitride spacers. A silica sphere of 113 nm of diameter was placed on the top window. (B) Calculation of the energy deposited to the silica particle *via* elastic and inelastic interactions of the incident electrons (in keV) for a frame acquired with a (S)TEM operated at 200 keV with 1.58 nm pixel size, 10 pA of beam current and $16 \mu\text{s}$ dwell time. The pixel size of the energy distribution corresponds to the pixel size used during imaging. The energy values indicate the deposited energy on the silica sphere from the electrons initially incident on that pixel. (C) Absorbed energy per unit volume of a silica particle located at the top SiN window for a number of electron beam currents with the previous imaging conditions. (D) Absorbed energy per unit volume of a silica particle located at different depths from the top SiN window for the case of 1 pA beam current.

water. The concentration of radicals under electron irradiation of water can be approximated for both our solvents with the widely used model of Schneider *et al.* (2014).³⁴ The results as a function of the electron dose rate can be found in Figure S6. The radical species that becomes more prevalent with increasing pH under our dose rates are hydrated electrons (e_{aq}^-). We then studied in detail the expansion phase in the absence, or in the presence, of a e_{aq}^- scavenger (potassium persulfate, $\text{K}_2\text{S}_2\text{O}_8$, 100 mM) under (S)TEM illumination ($370 e^- \text{nm}^{-2} \text{s}^{-1}$). No difference in the velocity or the extent of the expansion was observed between water or 100 mM NaOH when $\text{K}_2\text{S}_2\text{O}_8$ was present (Figure S7). In consequence, our results indicate that the initial composition of the solvent was more relevant than the formation of radiolysis radicals by the electron beam, in contrast to the accelerated dissolution phase. We then assessed whether the expansion phase was more likely driven by ionization or by direct knock-on events between the electrons and the silica network. To this end, AAC silica particles were imaged in (S)TEM mode with a TEM operated at 120 keV. Lower acceleration voltages of the microscope and, therefore, lower energies result in a lower direct knock-on cross section.⁵⁵ For example, the knock-on threshold for silicon is around 140 keV,⁵⁶ and no knock-on damage would happen for electrons having an energy below this threshold. Expansion and accelerated dissolution were also observed under 120 keV (S)TEM ($960 e^- \text{nm}^{-2} \text{s}^{-1}$) illumination in water (Figure S8A). The extent of the expansion matched the expansion observed with 200 keV imaging and did not differ much in speed. The expansion phase was also faster and more severe in 100 mM NaOH (Figure S8B). That the expansion phase persists also under illumination of electrons with significantly less energy suggests that the underlying mechanism is likely based on bond

ionization. Although the temperature in the liquid cell during imaging is supposed to increase only marginally,⁵⁷ silica solubility in water depends on the temperature, and thus, we also assessed this parameter. To this end, we imaged AAC silica nanoparticles in water by performing in situ heating LC-(S)TEM experiments ($500 e^- \text{nm}^{-2} \text{s}^{-1}$) with a range (up to 90°C) of temperatures greatly exceeding the potential local temperature increase induced by the electron beam (Figure S9). No difference in the expansion and accelerated dissolution was observed between different temperatures, proving the effect of local heating in our experiments negligible.

3.3. Monte-Carlo Simulations of the Electron Trajectories during LC-(S)TEM Imaging of Silica Particles in Water. So far, the effects of electron beam irradiation on silica particles in LC-(S)TEM experiments discussed in the literature were in terms of the radiolysis of the solvent. However, this interpretation does not fully explain the expansion/dissolution behavior. Our DLS results show that although a higher pH resulted in increased etching rates, this resulted in a small increase in the etching rate above 100 mM NaOH. Lower pH values resulted in slower etching. Therefore, changes in the concentration of OH^- ions cannot fully explain our observations. Additionally, the formation of reducing radicals is also supposed to be lower if the pH of the irradiated solution is high.³⁴ If the expansion was mediated by such species, it would depend on the electron dose rate and it would be reduced at higher starting pH. It is quite clear that chemical modifications of the siloxane structure as caused by the energy deposited by the electron beam also have to play an important role. Here, we propose that the direct interaction between the electron beam and the silica network is the main driver of the expansion/dissolution behavior. To explore this possibility, the deposited energy in the particles during our LC-(S)TEM

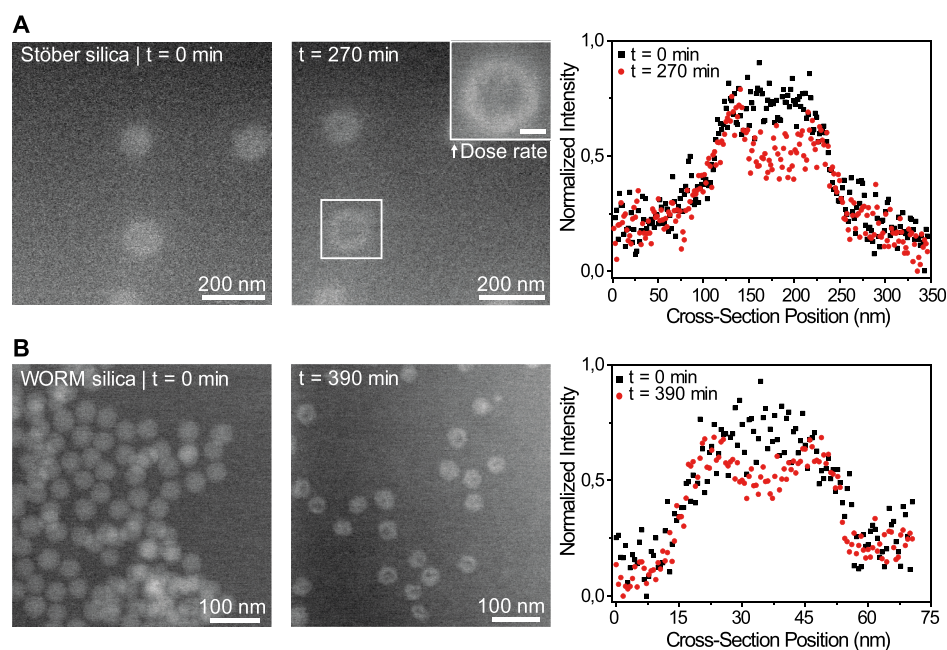


Figure 5. *In situ* etching of silica model nanoparticles by exposure to a 100 mM NaOH aqueous solution with a flow rate of $5 \mu\text{L}\cdot\text{min}^{-1}$. (A) Stöber silica. Particles became hollow when exposed to a flow of 100 mM NaOH. right: The intensity profile along the nanoparticle shown in the inset. No expansion was observed (a total accumulated dose of $1.4 \times 10^4 \text{ e}^- \text{nm}^{-2}$). Inset scale bar: 50 nm. (B) WORM silica nanospheres under a flow of 100 mM NaOH. Due to the small size of the particles (40 nm), our results indicate that the silica network was strongly affected even in a single frame (a total accumulated dose of $1.5 \times 10^3 \text{ e}^- \text{nm}^{-2}$). Therefore, different areas needed to be imaged to study how WORM silica nanospheres etched under basic conditions. Particles showed hollowing after 390 min of exposure to the basic solution. right: Intensity profiles of two selected nanoparticles showing the formation of a hollow volume inside the particle, with minimal change in total size of the nanoparticle. Similarly as reported before for these particles systems.¹⁶

experiments was assessed. The energy deposited per unit volume was compared to the energy needed to affect the siloxane bonds to assess whether this effect is relevant for typical LC-(S)TEM imaging conditions. If the electron beam can affect a significant number of bonds in the structure of the silica network during imaging, silica solubility may increase and etching may be favored. The loss of condensation all over the particles due to the beam-induced excitation of siloxane bonds could then explain their expansion.

The energy that was deposited per cubic nanometer (nm^3) of silica during a LC-(S)TEM experiment was modeled by means of Monte-Carlo simulations with the software CASINO 3.3.⁵⁸ This software simulates the electron paths during (S)TEM imaging through a given sample. The elastic scattering interactions are treated as discrete events, and the inelastic interactions are treated with an energy loss model. Secondary electron generation is also considered. A 3D model of a simplified liquid cell environment was defined to model our experiments. The simulated geometry consisted of two silicon nitride windows of 50 nm thickness that enclosed a $1 \mu\text{m}$ thick layer of water. In this water volume, we positioned a silica sphere with a 113 nm diameter to emulate our AAC silica particles. The position of the center of the particle was chosen such that the particle was attached to the top window (Figure 4A). From the pathways of all the simulated electrons, CASINO calculates the total energy absorbed by every component of the simulated volume. The beam parameters were matched with our experimental conditions: the distance between irradiated points was set to be the experimental pixel size, the number of electrons per scanned point was determined as previously done in the literature from the beam current and the dwell time,^{59,60} the beam was focused on

the particle, and a beam convergence semi-angle of 20 mrad was used.

The energy absorbed per frame by the silica particle for the electrons used to generate a given pixel (1.58 nm pixel size, 1024×1024 pixels, 10 pA beam current and $16 \mu\text{s}$ dwell time) can be seen in Figure 4B. The binding energy of the Si–O bond is 4.60 eV,⁶¹ and there are approximately 216 Si–O bonds in 1 nm^3 (if we assume perfectly condensed silica, which is not the case for all kind of silica nanoparticles). The following rule of thumb can be derived from CASINO simulations for small silica particles located on the top window of a liquid cell: around 12 eV of energy is deposited per nm^3 of silica, per pA of beam current for a frame acquired with $1 \mu\text{s}$ dwell time and with 1 nm^2 pixel size. However, for our experimental conditions, the total absorbed energy per frame per nm^3 could be range from several keV to several MeV (Figure 4C). Furthermore, we see that the deposited energy on the particle barely depended on the depth of the particles in the liquid cell and on whether the beam was focused on the particles or not (Figure 4D). Beam current, dwell time, and pixel size are therefore the main parameters that need to be optimized to reduce the cumulative dose per frame. This highlights the potential of direct electron detectors, which are nowadays routinely used in cryo-EM experiments because of their ability to gather information from a sample at much lower irradiation levels ($\sim 1 \text{ e}^- \text{Å}^{-2}$).^{62,63}

The main contributions to the absorbed energy are the inelastic interactions between the electrons of the beam and those of the material, as the inelastic scattering cross-section is larger than the elastic scattering cross-section for Si and especially for O for 200 keV electrons.⁶⁴ The inelastic scattering of the electrons can promote radiolytic processes

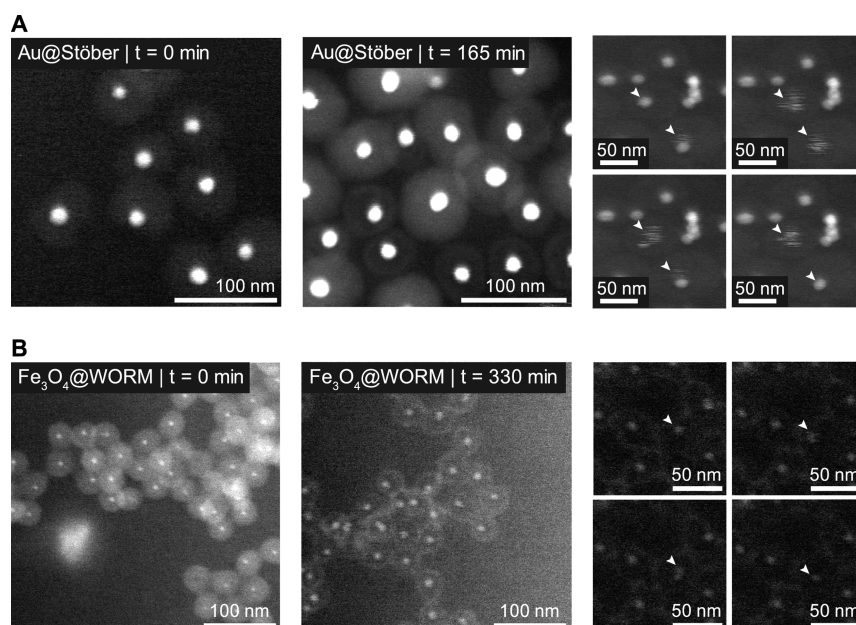


Figure 6. *In situ* etching of core–shell metal(oxide)–silica nanoparticles by exposure to a 100 mM NaOH aqueous solution with a flow rate of 5 $\mu\text{L}\cdot\text{min}^{-1}$. (A) Au–silica. (B) Wet etching of Fe_3O_4 core/WORM silica core/shell nanoparticles into yolk–shell particles under the flow of a basic aqueous solution. At the left, particles at the start of the experiment. At the center, yolk–shell particles formed after 165 and 330 min of exposure to the basic solution by the etching of the silica shell. Different areas were imaged in both (A) and (B) due to beam sensitivity (total accumulated dose of $1.5 \times 10^3 \text{ e}^- \cdot \text{nm}^{-2}$). At the right, experimental observation of the “free” diffusion of the catalytic cores. The white arrows highlight single cores rattling through the void of the yolk–shell particle.

in the irradiated material.^{65,66} The decay of the electronic excitations caused by radiolysis can result in breaking of chemical bonds and may result in atomic displacements in a network as energy can be transmitted to the atom nuclei *via* phonons and excitons. Importantly, not every excitation decay results in atomic displacements, as a broken chemical bond does not directly imply a gain in energy sufficient to displace an atom over the surrounding energy barriers.⁶⁵ In silicates, the cross-section for radiolytic atom displacements is 10 times higher than that for direct elastic events.⁶⁷ In silica, electron irradiation promotes the excitation of siloxane bonds, which in turn can result in the formation of point defects and the loss of connectivity of the silica network.^{66,68}

Radiolysis damage is typically assumed to be proportional to the energy deposited by radiation.⁶⁹ Deposited energies on quartz (crystalline silica) of a few hundred $\text{eV}\cdot\text{nm}^{-3}$ *via* ion beam bombardment have been shown to cause amorphization.⁷⁰ Ion bombardment has also been shown to induce the deformation of spherical particles;⁷¹ however, the energies involved are in the MeV range which is quite different from the electron beams used in TEM, and quartz amorphization has been well described for electron irradiation.⁶⁸ The energy absorbed by silica can be compared to the landscape of energies that have to be reached to displace an atom in the silica network. The energy needed to displace an O atom or a Si atom in the silica network is of the order of a few eV,⁷² and electron irradiation of SiO_2 films has been shown to displace O atoms, reducing the SiO_2 film into more pure Si areas through the formation of point defects.^{55,66} Therefore, during LC-(S)TEM experiments, the typical amounts of energy deposited into the silica network can be up to orders of magnitude higher than the energy needed to strongly affect the siloxane bonds. Such bond breaking (and atomic displacement) events taking place in a particle dispersed in an aqueous NaOH medium will,

with no doubt, lead to the easier dissolution of the silica network. Consequently, our results could be explained by an increase in the susceptibility of the silica network to etching by the aqueous base solution as a result of the direct electron beam effects on the material. Additionally, scavenging some of the reducing radicals that are produced by the electron beam was shown to slightly stabilize silica in liquid cell experiments.³¹ However, it is likely that these effects are small compared to the increased solubility by the cleavage of siloxane bonds.

3.4. *In situ* Study of the Wet Etching of SiO_2 and Metal(Oxide)@ SiO_2 Nanoparticles. We first characterized the etching of Stöber and WORM silica nanoparticles (Figure 5) by exposing them to a solution of 100 mM NaOH (5 $\mu\text{L}\cdot\text{min}^{-1}$). Stöber silica nanoparticles showed an inhomogeneous etching pattern, in accordance with their internal distribution of silica condensation levels (Figures 5A and S10).¹⁶ This process took place at different time scales for different particles and was in contrast to the etching patterns of Stöber silica during LC-(S)TEM experiments under higher electron dose rates and cumulative electron doses.³¹ We minimized the cumulative electron dose by imaging with an electron dose rate of $61 \text{ e}^- \cdot \text{nm}^{-2} \text{ s}^{-1}$, 1.58 nm pixels, 1024×1024 pixels frames, 24 μs dwell time, and 30 min blanks between frames (a total accumulated dose of $1.4 \times 10^4 \text{ e}^- \cdot \text{nm}^{-2}$ for Stöber silica nanoparticles and $1.5 \times 10^3 \text{ e}^- \cdot \text{nm}^{-2}$ for WORM silica nanoparticles). Once the hollow structures became evident, a final frame was taken with $260 \text{ e}^- \cdot \text{nm}^{-2} \text{ s}^{-1}$ to get better detail (Figure 5A, inset). By comparing the intensity profile of a cross section of a single particle, it can be readily seen that these imaging conditions did not induce any expansion during the etching process, correctly characterizing the final product of the wet chemical etching of Stöber silica (Figure 5A, right panel).

Studying WORM silica was more difficult than studying AAC and Stöber silica spheres, as the size of the nanoparticles was smaller (40 nm). This made it more challenging to image such nanospheres at low total accumulated electron doses, as it required both the dose rate and the magnification to be higher ($1.5 \times 10^3 \text{ e}^- \text{ nm}^{-2}$, 0.55 nm pixel size, 24 μs dwell time). Therefore, for silica particles of this size range, it is advisable to image the same area only once. Making use of this knowledge, we followed the evolution of monodispersed WORM silica spheres under a flow of aqueous 100 mM NaOH ($5 \mu\text{L} \cdot \text{min}^{-1}$) by imaging different areas over time (Figure 5B). WORM silica spheres became hollow after 390 min of exposure to the basic solution, consistent with their behavior under hydrothermal treatments.²⁵ It is relevant to mention here that this particle size limit could be lowered by utilizing detectors with higher sensitivities that allow imaging with lower electron dose rates and thus with a lower cumulative electron dose per frame. However, there are three factors to be considered: first, if following a single particle is of paramount importance, the particles could be imaged first in water, in which we have shown that the beam damage is lower. Then, water and the etching media could be alternated by making use of dedicated liquid cell holders with dual flow capabilities. Second, although for this particle size one cannot, in principle, follow the process in the etching media at the single particle level under our lower beam intensity settings, it is still possible to characterize the process when the particles are relatively monodisperse, as their behavior should not differ much from particle to particle. Third, we characterized the final product without going through purification, cleaning, or any drying steps, which could potentially change the particle shape and would stop any dynamics going on inside the particles. This last factor in itself is already a powerful reason to aim for routine liquid cell (S)TEM experiments in order to follow the wet etching process of nanoparticles.

The formation of yolk–shell structures from metal(oxide)@silica core–shell nanoparticles could also be studied with the methods described previously. Yolk–shell nanoparticles consisting of a catalytically or surface enhanced Raman scattering active cores surrounded by a void and encapsulated by a porous support are known to show superior catalytic and sensing activity in many scenarios.^{73,74} This increased efficiency comes from the role of the hollow shell as a micro/nanoreactor, offering a number of advantages such as: prevention of particle sintering, controlled diffusion rates through the shell pores, and homogeneous environments in the void surrounding the catalyst or sensing particle. The synthesis of such particles usually consists of a hard template-based synthesis of core–shell particles and the subsequent removal of material to form a void between the core template and the shell. Here, we investigate the void formation step for Au@Stöber silica and Fe_3O_4 @WORM silica core–shell particles upon wet etching of the silica shell with a NaOH aqueous solution (Figure 6); both these two systems stand as a model for a broad range of nanocore–silica–shell particles. We showed that by slightly etching the Stöber (Figure 6A) and the WORM (Figure 6B) silica shells with a basic solution, well-defined yolk–shell particles are obtained. Furthermore, the Au and Fe_3O_4 cores were found to diffuse in the void once such etching was completed. This opens the door to fully treat the surface of the catalyst once the yolk is formed and also indicates that the behavior of the catalyst could be manipulated

separately from the shell in the liquid phase *via* external fields, as it has been reported for similar structures.⁷⁵

4. CONCLUSIONS

The wet etching of silica and metal(oxide)@silica nanoparticles in an aqueous NaOH solution was studied by means of *in situ* LC-(S)TEM. We exploited the slow and gradual etching of AAC silica spheres in basic solutions to investigate and mitigate the electron beam effects during LC-(S)TEM studies of silica in aqueous and basic aqueous solutions. Our results pinpoint the cumulative electron dose on silica particles during *in situ* LC-(S)TEM experiments as the critical parameter determining whether the observations will diverge from *ex situ* etching behavior, and show that conditions can be found where the effects can be neglected. Under the conditions where the effects of the electron beam did affect the etching, we report that silica was first found to expand and then dissolve when irradiated in an aqueous environment and that the extent of such expansion was directly correlated to the cumulative electron dose on the imaging area, independent of the used electron dose rate. We showed that this behavior was not the result of changes in the pH of the solution. Furthermore, the expansion and dissolution phenomena were more pronounced under basic conditions. The formation of reducing radicals is assumed to be lower at basic conditions,³⁴ and therefore, we conclude that the reported expansion cannot be explained by the presence of water radiolysis products. By performing simulations of the electron beam energy loss, we conclude that the energy absorbed per unit volume per frame by a silica nanoparticle of around a hundred nanometers on the top window of a liquid cell could be up to orders of magnitude higher than the energy needed to directly break bonds in the silica siloxane network. We propose that the direct effects of the electron beam on the silica network, make it more susceptible to etching by the OH^- ions in solution and the water radiolysis products. If the energy deposited on the nanoparticles during LC-(S)TEM experiments alters the rate of chemical processes happening between the nanoparticle and the solvent, then the cumulative electron dose (and the electron dose history prior to data acquisition) must be carefully controlled and reported to achieve reliable *in situ* studies on chemical reactions in LC-(S)TEM experiments. Using this knowledge, we reliably characterized the wet etching behavior of multiple silica-based model systems: Stöber silica, WORM silica, and Au@Stöber silica, and Fe_3O_4 @WORM silica core–shell nanoparticles under conditions where the effects of the electron beam could be neglected. We showed that LC-(S)TEM can correctly reproduce the expected etching patterns for Stöber and WORM silica as well as the formation of yolk–shell structures from Au@Stöber silica and Fe_3O_4 @WORM silica core–shell nanoparticles as reported before in the literature.^{76,77} Furthermore, we showed how the catalyst core became a movable particle inside the shell as the yolk was formed, opening the door to extensive post-treatments of such core-silica-shell systems as well as to manipulations of the movable core with external fields. Our results might be applicable to similar systems. For example, expansion in water under electron beam irradiation has also been reported for niobic acid nanoparticles.⁵³ Accelerated dissolution has also been reported for many other oxides (CeO_2 , VO_2 , FeO_3 , CuO , MgO , and Al_2O_3).^{52,53} Future studies following our methodology are invited to consider whether the approach presented in the current paper also allows the imaging of such materials

and their etching processes without influence of the electron beam.

■ ASSOCIATED CONTENT

SI Supporting Information

The Supporting Information is available free of charge at <https://pubs.acs.org/doi/10.1021/acsanm.0c02771>.

Correlation between TEOS volume used during synthesis and final size of AAC silica spheres; final sizes of AAC silica particles after *ex situ* etching for a range of NaOH concentrations; progression of the polydispersity of AAC silica spheres in time during *ex situ* etching in NaOH; Stöber and AAC silica nanoparticles' *ex situ* etching by HF; free-hand lithography of AAC silica spheres in water; calculations of steady-state radiolysis radicals in water and 100 mM NaOH; expansion phase of AAC silica spheres in water and 100 mM NaOH in the presence and absence of potassium persulfate; behavior of AAC silica spheres under 120 keV (S)TEM illumination in water and 100 mM NaOH; And behavior of AAC silica spheres in water at different temperatures under 200 keV (S)TEM illumination (PDF)

Electron beam-induced expansion of AAC silica particles in water ($570 \text{ e}^- \text{ nm}^{-2} \text{ s}^{-1}$) observed during LC-(S)TEM experiments (AVI)

Electron beam-induced expansion of AAC silica particles in water ($1100 \text{ e}^- \text{ nm}^{-2} \text{ s}^{-1}$) observed during LC-(S)TEM experiments (AVI)

Electron beam-induced expansion of AAC silica particles in water ($2300 \text{ e}^- \text{ nm}^{-2} \text{ s}^{-1}$) observed during LC-(S)TEM experiments (AVI)

Electron beam induced expansion of AAC silica particles in 100 mM NaOH ($31 \text{ e}^- \text{ nm}^{-2} \text{ s}^{-1}$) observed during LC-(S)TEM experiments (AVI)

Electron beam induced expansion of AAC silica particles in 100 mM NaOH ($520 \text{ e}^- \text{ nm}^{-2} \text{ s}^{-1}$) observed during LC-(S)TEM experiments (AVI)

Electron beam induced expansion of AAC silica particles in 100 mM NaOH ($2300 \text{ e}^- \text{ nm}^{-2} \text{ s}^{-1}$) observed during LC-(S)TEM experiments (AVI)

Electron beam induced expansion of AAC silica particles in 100 mM NaOH ($3400 \text{ e}^- \text{ nm}^{-2} \text{ s}^{-1}$) observed during LC-(S)TEM experiments (AVI)

Electron beam induced expansion of AAC silica particles in 100 mM NaOH ($41 \text{ e}^- \text{ nm}^{-2} \text{ s}^{-1}$) observed during LC-(S)TEM experiments (AVI)

■ AUTHOR INFORMATION

Corresponding Authors

Alfons van Blaaderen – *Soft Condensed Matter, Debye Institute for Nanomaterials Science, Utrecht University, Utrecht 3584 CC, The Netherlands*;
Email: A.vanBlaaderen@uu.nl

Marijn A. van Huis – *Soft Condensed Matter, Debye Institute for Nanomaterials Science, Utrecht University, Utrecht 3584 CC, The Netherlands*; orcid.org/0000-0002-8039-2256;
Email: M.A.vanHuis@uu.nl

Authors

Albert Grau-Carbonell – *Soft Condensed Matter, Debye Institute for Nanomaterials Science, Utrecht University,*

Utrecht 3584 CC, The Netherlands; orcid.org/0000-0002-8901-389X

Sina Sadighikia – *Soft Condensed Matter, Debye Institute for Nanomaterials Science, Utrecht University, Utrecht 3584 CC, The Netherlands*

Tom A. J. Welling – *Soft Condensed Matter, Debye Institute for Nanomaterials Science, Utrecht University, Utrecht 3584 CC, The Netherlands*

Relinde J. A. van Dijk-Moes – *Soft Condensed Matter, Debye Institute for Nanomaterials Science, Utrecht University, Utrecht 3584 CC, The Netherlands*

Ramakrishna Kotni – *Soft Condensed Matter, Debye Institute for Nanomaterials Science, Utrecht University, Utrecht 3584 CC, The Netherlands*

Maarten Bransen – *Soft Condensed Matter, Debye Institute for Nanomaterials Science, Utrecht University, Utrecht 3584 CC, The Netherlands*; orcid.org/0000-0002-4002-5291

Complete contact information is available at:

<https://pubs.acs.org/doi/10.1021/acsanm.0c02771>

■ Author Contributions

A.G.-C. and S.S. contributed equally to this work. A.G.-C. and S.S. performed the LC-(S)TEM experiments, nanoparticle synthesis, data analysis, and manuscript preparation. T.A.J.W. assisted in the LC-(S)TEM experiments. R.J.A.v.D.-M., R.K., and M.B. performed nanoparticle synthesis. A.v.B. and M.A.v.H. designed and supervised the experiments and interpreted data. All authors have critically read the manuscript.

■ Notes

The authors declare no competing financial interest.

■ ACKNOWLEDGMENTS

This project received funding from the European Research Council (ERC) *via* the ERC Consolidator Grant NANO-INSITU (grant no. 683076). The authors also acknowledge funding from the NWO-TTW Perspectief Program “Understanding Processes Using Operando Nanoscopy,” project UPON-B3 (no. 14206). R.K. and M.B. acknowledge funding from the Netherlands Center for Multiscale Catalytic Energy Conversion (MCEC), an NWO Gravitation programme funded by the Ministry of Education, Culture, and Science of the government of the Netherlands.

■ REFERENCES

- (1) Gao, X.; He, J.; Deng, L.; Cao, H. Synthesis and Characterization of Functionalized Rhodamine B-Doped Silica Nanoparticles. *Opt. Mater.* **2009**, *31*, 1715–1719.
- (2) Tovmachenko, O. G.; Graf, C.; van den Heuvel, D. J.; van Blaaderen, A.; Gerritsen, H. C. Fluorescence Enhancement by Metal-Core/Silica-Shell Nanoparticles. *Adv. Mater.* **2006**, *18*, 91–95.
- (3) Horozov, T. S.; Aveyard, R.; Binks, B. P.; Clint, J. H. Structure and Stability of Silica Particle Monolayers at Horizontal and Vertical Octane-Water Interfaces. *Langmuir* **2005**, *21*, 7405–7412.
- (4) Nakamura, M.; Shono, M.; Ishimura, K. Synthesis, Characterization, and Biological Applications of Multifluorescent Silica Nanoparticles. *Anal. Chem.* **2007**, *79*, 6507–6514.
- (5) Graf, C.; Vossen, D. L. J.; Imhof, A.; van Blaaderen, A. A General Method to Coat Colloidal Particles with Silica. *Langmuir* **2003**, *19*, 6693–6700.
- (6) van Blaaderen, A.; van Geest, J.; Vrij, A. Monodisperse Colloidal Silica Spheres from Tetraalkoxysilanes: Particle Formation and Growth Mechanism. *J. Colloid Interface Sci.* **1992**, *154*, 481–501.

- (7) van Blaaderen, A.; Vrij, A. Synthesis and Characterization of Colloidal Dispersions of Fluorescent, Monodisperse Silica Spheres. *Langmuir* **1992**, *8*, 2921–2931.
- (8) Stöber, W.; Fink, A.; Bohn, E. Controlled Growth of Monodisperse Silica Spheres in the Micron Size Range. *J. Colloid Interface Sci.* **1968**, *26*, 62–69.
- (9) Arriagada, F. J.; Osseo-Asare, K. Synthesis of Nanosize Silica in a Nonionic Water-in-Oil Microemulsion: Effects of the Water/Surfactant Molar Ratio and Ammonia Concentration. *J. Colloid Interface Sci.* **1999**, *211*, 210–220.
- (10) Arriagada, F. J.; Osseo-Asare, K. Phase and Dispersion Stability Effects in the Synthesis of Silica Nanoparticles in a Non-Ionic Reverse Microemulsion. *Colloids Surf.* **1992**, *69*, 105–115.
- (11) Koole, R.; van Schooneveld, M. M.; Hilhorst, J.; de Mello Donegá, C.; 't Hart, D. C.; van Blaaderen, A.; Vanmaekelbergh, D.; Meijerink, A. On the Incorporation Mechanism of Hydrophobic Quantum Dots in Silica Spheres by a Reverse Microemulsion Method. *Chem. Mater.* **2008**, *20*, 2503–2512.
- (12) Osseo-Asare, K.; Arriagada, F. J. Preparation of SiO₂ Nanoparticles in a Non-Ionic Reverse Micellar System. *Colloids Surf.* **1990**, *50*, 321–339.
- (13) Shahabi, S.; Treccani, L.; Rezwani, K. A Comparative Study of Three Different Synthesis Routes for Hydrophilic Fluorophore-Doped Silica Nanoparticles. *J. Nanopart. Res.* **2016**, *18*, 28.
- (14) Yokoi, T.; Wakabayashi, J.; Otsuka, Y.; Fan, W.; Iwama, M.; Watanabe, R.; Aramaki, K.; Shimojima, A.; Tatsumi, T.; Okubo, T. Mechanism of Formation of Uniform-Sized Silica Nanospheres Catalyzed by Basic Amino Acids. *Chem. Mater.* **2009**, *21*, 3719–3729.
- (15) Yokoi, T.; Karouji, T.; Ohta, S.; Kondo, J. N.; Tatsumi, T. Synthesis of Mesoporous Silica Nanospheres Promoted by Basic Amino Acids and their Catalytic Application. *Chem. Mater.* **2010**, *22*, 3900–3908.
- (16) Wong, Y. J.; Zhu, L.; Teo, W. S.; Tan, Y. W.; Yang, Y.; Wang, C.; Chen, H. Revisiting the Stöber method: Inhomogeneity in Silica Shells. *J. Am. Chem. Soc.* **2011**, *133*, 11422–11425.
- (17) Yokoi, T.; Sakamoto, Y.; Terasaki, O.; Kubota, Y.; Okubo, T.; Tatsumi, T. Periodic Arrangement of Silica Nanospheres Assisted by Amino Acids. *J. Am. Chem. Soc.* **2006**, *128*, 13664–13665.
- (18) Fouilloux, S.; Taché, O.; Spalla, O.; Thill, A. Nucleation of Silica Nanoparticles Measured in Situ during Controlled Supersaturation Increase. Restructuring toward a Monodisperse Nonspherical Shape. *Langmuir* **2011**, *27*, 12304–12311.
- (19) Carcouët, C. C. M. C.; van de Put, M. W. P.; Mezari, B.; Magusin, P. C. M. M.; Laven, J.; Bomans, P. H. H.; Friedrich, H.; Esteves, A. C. C.; Sommerdijk, N. A. J. M.; van Benthem, R. A. T. M. Nucleation and Growth of Monodisperse Silica Nanoparticles. *Nano Lett.* **2014**, *14*, 1433–1438.
- (20) Chang, C.-L.; Fogler, H. S. Controlled Formation of Silica Particles from Tetraethyl Orthosilicate in Nonionic Water-in-Oil Microemulsions. *Langmuir* **1997**, *13*, 3295–3307.
- (21) Davis, T. M.; Snyder, M. A.; Krohn, J. E.; Tsapatsis, M. Nanoparticles in Lysine-Silica Sols. *Chem. Mater.* **2006**, *18*, 5814–5816.
- (22) van Blaaderen, A.; Kentgens, A. P. M. Particle Morphology and Chemical Microstructure of Colloidal Silica Spheres Made from Alkoxysilanes. *J. Non-Cryst. Solids* **1992**, *149*, 161–178.
- (23) Brinker, C. J. Hydrolysis and Condensation of Silicates: Effects on Structure. *J. Non-Cryst. Solids* **1988**, *100*, 31–50.
- (24) Bazula, P. A.; Arnal, P. M.; Galeano, C.; Zibrowius, B.; Schmidt, W.; Schüth, F. Highly Microporous Monodisperse Silica Spheres Synthesized by the Stöber Process. *Microporous Mesoporous Mater.* **2014**, *200*, 317–325.
- (25) Lin, C.-H.; Chang, J.-H.; Yeh, Y.-Q.; Wu, S.-H.; Liu, Y.-H.; Mou, C.-Y. Formation of Hollow Silica Nanospheres by Reverse Microemulsion. *Nanoscale* **2015**, *7*, 9614–9626.
- (26) Iler, R. K. *The Chemistry of Silica, Solubility, Polymerization, Colloid and Surface Properties, and Biochemistry*; John Wiley & Sons, Ltd. New York, Chichester, Brisbane, Toronto, Singapore, 1979.
- (27) Sjöberg, S. Silica in Aqueous Environments. *J. Non-Cryst. Solids* **1996**, *196*, 51–57.
- (28) Aabdin, Z.; Xu, X. M.; Sen, S.; Anand, U.; Král, P.; Holsteyns, F.; Mirsaidov, U. Transient Clustering of Reaction Intermediates during Wet Etching of Silicon Nanostructures. *Nano Lett.* **2017**, *17*, 2953–2958.
- (29) Jiang, Y.; Zhu, G.; Lin, F.; Zhang, H.; Jin, C.; Yuan, J.; Yang, D.; Zhang, Z. In Situ Study of Oxidative Etching of Palladium Nanocrystals by Liquid Cell Electron Microscopy. *Nano Lett.* **2014**, *14*, 3761–3765.
- (30) Jiang, Y.; Zhu, G.; Dong, G.; Lin, F.; Zhang, H.; Yuan, J.; Zhang, Z.; Jin, C. Probing the Oxidative Etching Induced Dissolution of Palladium Nanocrystals in Solution by Liquid Cell Transmission Electron Microscopy. *Micron* **2017**, *97*, 22–28.
- (31) Meijerink, M. J.; Spiga, C.; Hansen, T. W.; Damsgaard, C. D.; de Jong, K. P.; Zečević, J. Nanoscale Imaging and Stabilization of Silica Nanospheres in Liquid Phase Transmission Electron Microscopy. *Part. Part. Syst. Charact.* **2019**, *36*, 1800374.
- (32) Hauwiler, M. R.; Frechette, L. B.; Jones, M. R.; Ondry, J. C.; Rotskoff, G. M.; Geissler, P.; Alivisatos, A. P. Unraveling Kinetically-Driven Mechanisms of Gold Nanocrystal Shape Transformations Using Graphene Liquid Cell Electron Microscopy. *Nano Lett.* **2018**, *18*, 5731–5737.
- (33) Hauwiler, M. R.; Ondry, J. C.; Chan, C. M.; Khandekar, P.; Yu, J.; Alivisatos, A. P. Gold Nanocrystal Etching as a Means of Probing the Dynamic Chemical Environment in Graphene Liquid Cell Electron Microscopy. *J. Am. Chem. Soc.* **2019**, *141*, 4428–4437.
- (34) Schneider, N. M.; Norton, M. M.; Mendel, B. J.; Grogan, J. M.; Ross, F. M.; Bau, H. H. Electron-Water Interactions and Implications for Liquid Cell Electron Microscopy. *J. Phys. Chem. C* **2014**, *118*, 22373–22382.
- (35) Woehl, T. J.; Abellan, P. Defining the Radiation Chemistry during Liquid Cell Electron Microscopy to Enable Visualization of Nanomaterial Growth and Degradation Dynamics. *J. Microsc.* **2017**, *265*, 135–147.
- (36) Liao, H.-G.; Cui, L.; Whitlam, S.; Zheng, H. Real-Time Imaging of Pt₃Fe Nanorod Growth in Solution. *Science* **2012**, *336*, 1011–1014.
- (37) Moser, T. H.; Mehta, H.; Park, C.; Kelly, R. T.; Shokuhfar, T.; Evans, J. E. The Role of Electron Irradiation History in Liquid Cell Transmission Electron Microscopy. *Sci. Adv.* **2018**, *4*, No. eaaq1202.
- (38) Wang, M.; Park, C.; Woehl, T. J. Quantifying the Nucleation and Growth Kinetics of Electron Beam Nanochemistry with Liquid Cell Scanning Transmission Electron Microscopy. *Chem. Mater.* **2018**, *30*, 7727–7736.
- (39) Jungjohann, K. L.; Bliznakov, S.; Sutter, P. W.; Stach, E. A.; Sutter, E. A. In Situ Liquid Cell Electron Microscopy of the Solution Growth of Au-Pd Core-Shell Nanostructures. *Nano Lett.* **2013**, *13*, 2964–2970.
- (40) Yuk, J. M.; Park, J.; Ercius, P.; Kim, K.; Hellebusch, D. J.; Crommie, M. F.; Lee, J. Y.; Zettl, A.; Alivisatos, A. P. High-Resolution EM of Colloidal Nanocrystal Growth Using Graphene Liquid Cells. *Science* **2012**, *336*, 61–64.
- (41) Abellan, P.; Moser, T. H.; Lucas, I. T.; Grate, J. W.; Evans, J. E.; Browning, N. D. The Formation of Cerium(III) Hydroxide Nanoparticles by a Radiation Mediated Increase in Local pH. *RSC Adv.* **2017**, *7*, 3831–3837.
- (42) Abellan, P.; Woehl, T. J.; Parent, L. R.; Browning, N. D.; Evans, J. E.; Arslan, I. Factors Influencing Quantitative Liquid (Scanning) Transmission Electron Microscopy. *Chem. Commun.* **2014**, *50*, 4873–4880.
- (43) Shahabi, S.; Treccani, L.; Rezwani, K. Amino Acid-Catalyzed Seed Regrowth Synthesis of Photostable High Fluorescent Silica Nanoparticles with Tunable Sizes for Intracellular Studies. *J. Nanopart. Res.* **2015**, *17*, 270.
- (44) Han, Y.; Jiang, J.; Lee, S. S.; Ying, J. Y. Reverse Microemulsion-Mediated Synthesis of Silica-Coated Gold and Silver Nanoparticles. *Langmuir* **2008**, *24*, 5842–5848.

- (45) Park, J.-e.; Grayfer, E. D.; Jung, Y.; Kim, K.; Wang, K.-K.; Kim, Y.-R.; Yoon, D.; Cheong, H.; Chung, H.-E.; Choi, S.-J. Photoluminescent Nanographitic/Nitrogen-Doped Graphitic Hollow Shells as a Potential Candidate for Biological Applications. *J. Mater. Chem. B* **2013**, *1*, 1229–1234.
- (46) Park, J.; An, K.; Hwang, Y.; Park, J.-G.; Noh, H.-J.; Kim, J.-Y.; Park, J.-H.; Hwang, N.-M.; Hyeon, T. Ultra-Large-Scale Syntheses of Monodisperse Nanocrystals. *Nat. Mater.* **2004**, *3*, 891–895.
- (47) Verch, A.; Pfaff, M.; de Jonge, N. Exceptionally Slow Movement of Gold Nanoparticles at a Solid/Liquid Interface Investigated by Scanning Transmission Electron Microscopy. *Langmuir* **2015**, *31*, 6956–6964.
- (48) Sadighikia, S.; Grau-Carbonell, A.; Welling, T.; Kotni, R.; Hagemans, F.; Imhof, A.; Huis, M.; van Blaaderen, A. Low-Dose Liquid Cell Electron Microscopy Investigation of the Complex Etching Mechanism of Rod-Shaped Silica Colloids. *Nano Select* **2020**, DOI: 10.1002/nano.202000060.
- (49) Zečević, J.; Hermannsdörfer, J.; Schuh, T.; de Jong, K. P.; de Jonge, N. Anisotropic Shape Changes of Silica Nanoparticles Induced in Liquid with Scanning Transmission Electron Microscopy. *Small* **2017**, *13*, 1602466.
- (50) Zheng, K.; Chengcai, W.; Cheng, Y.-Q.; Yue, Y.; Han, X.; Zhang, Z.; Shan, Z.; Mao, S.; Ye, M.; Yin, Y. Electron-Beam-Assisted Superplastic Shaping of Nanoscale Amorphous Silica. *Nat. Commun.* **2010**, *1*, 24.
- (51) Jiang, N. Note on In Situ (Scanning) Transmission Electron Microscopy Study of Liquid Samples. *Ultramicroscopy* **2017**, *179*, 81–83.
- (52) Lu, Y.; Geng, J.; Wang, K.; Zhang, W.; Ding, W.; Zhang, Z.; Xie, S.; Dai, H.; Chen, F.-R.; Sui, M. Modifying Surface Chemistry of Metal Oxides for Boosting Dissolution Kinetics in Water by Liquid Cell Electron Microscopy. *ACS Nano* **2017**, *11*, 8018–8025.
- (53) Meijerink, M. J.; de Jong, K. P.; Zečević, J. Assessment of Oxide Nanoparticle Stability in Liquid Phase Transmission Electron Microscopy. *Nano Res.* **2019**, *12*, 2355–2363.
- (54) Welling, T. A. J.; Sadighikia, S.; Watanabe, K.; Grau-Carbonell, A.; Bransen, M.; Nagao, D.; Van Blaaderen, A.; van Huis, M. A. Observation of Undamped 3D Brownian Motion of Nanoparticles Using Liquid-Cell Scanning Transmission Electron Microscopy. *Part. Syst. Charact.* **2020**, *37*, 2000003.
- (55) Neelisetty, K. K.; Mu, X.; Gutsch, S.; Vahl, A.; Molinari, A.; von Seggern, F.; Hansen, M.; Scherer, T.; Zacharias, M.; Kienle, L. Electron Beam Effects on Oxide Thin Films-Structure and Electrical Property Correlations. *Microsc. Microanal.* **2019**, *25*, 592–600.
- (56) Hudak, B. M.; Song, J.; Sims, H.; Troparevsky, M. C.; Humble, T. S.; Pantelides, S. T.; Snijders, P. C.; Lupini, A. R. Directed Atom-by-Atom Assembly of Dopants in Silicon. *ACS Nano* **2018**, *12*, 5873–5879.
- (57) Zheng, H.; Claridge, S. A.; Minor, A. M.; Alivisatos, A. P.; Dahmen, U. Nanocrystal Diffusion in a Liquid Thin Film Observed by in Situ Transmission Electron Microscopy. *Nano Lett.* **2009**, *9*, 2460–2465.
- (58) Demers, H.; Poirier-Demers, N.; Couture, A. R.; Joly, D.; Guilmain, M.; de Jonge, N.; Drouin, D. Three-Dimensional Electron Microscopy Simulation with the CASINO Monte Carlo Software. *Scanning* **2011**, *33*, 135–146.
- (59) de Jonge, N.; Poirier-Demers, N.; Demers, H.; Peckys, D. B.; Drouin, D. Nanometer-Resolution Electron Microscopy Through Micrometers-Thick Water Layers. *Ultramicroscopy* **2010**, *110*, 1114–1119.
- (60) Demers, H.; Poirier-Demers, N.; Drouin, D.; de Jonge, N. Simulating STEM Imaging of Nanoparticles in Micrometers-Thick Substrates. *Microsc. Microanal.* **2010**, *16*, 795–804.
- (61) Holleman, A. F.; Wiberg, E.; Wiberg, N.; Brewer, W.; Eagleson, M. L. *Textbook of Inorganic Chemistry*; Academic Press, 2001.
- (62) McMullan, G.; Faruqi, A. R.; Henderson, R. *Methods in Enzymology*, 1st ed.; Elsevier Inc., 2016; Vol. 579, pp 1–17.
- (63) Fujiyoshi, Y. In *Electron Crystallography of Soluble and Membrane Proteins: Methods and Protocols*; Schmidt-Krey, I., Cheng, Y., Eds.; Humana Press: Totowa, NJ, 2013; pp 103–118.
- (64) Jiang, N. Electron Beam Damage in Oxides: A Review. *Rep. Prog. Phys.* **2016**, *79*, 016501.
- (65) Kabler, M. N.; Williams, R. T. Vacancy-Interstitial Pair Production via Electron-Hole Recombination in Halide Crystals. *Phys. Rev. B* **1978**, *18*, 1948–1960.
- (66) Hobbs, L. W. Electron-Beam Sensitivity in Inorganic Specimens. *Ultramicroscopy* **1987**, *23*, 339–344.
- (67) Egerton, R. F. Mechanisms of Radiation Damage in Beam-Sensitive Specimens, for TEM Accelerating Voltages Between 10 and 300 kV. *Microsc. Res. Tech.* **2012**, *75*, 1550–1556.
- (68) Inui, H.; Mori, H.; Sakata, T.; Fujita, H. Electron Irradiation Induced Crystalline-to-Amorphous Transition in Quartz Single Crystals. *J. Non-Cryst. Solids* **1990**, *116*, 1–15.
- (69) Egerton, R. F. Radiation Damage to Organic and Inorganic Specimens in the TEM. *Micron* **2019**, *119*, 72–87.
- (70) Eby, R. K.; Ewing, R. C.; Birtcher, R. C. The Amorphization of Complex Silicates by Ion-Beam Irradiation. *J. Mater. Res.* **1992**, *7*, 3080–3102.
- (71) Vossen, D. L. J.; Fific, D.; Penninkhof, J.; van Dillen, T.; Polman, A.; van Blaaderen, A. Combined Optical Tweezers/Ion Beam Technique to Tune Colloidal Masks for Nanolithography. *Nano Lett.* **2005**, *5*, 1175–1179.
- (72) Estreicher, S. K.; Backlund, D. J.; Carbogno, C.; Scheffler, M. Activation Energies for Diffusion of Defects in Silicon: The Role of the Exchange-Correlation Functional. *Angew. Chem., Int. Ed.* **2011**, *50*, 10221–10225.
- (73) Wang, X.; Feng, J.; Bai, Y.; Zhang, Q.; Yin, Y. Synthesis, Properties, and Applications of Hollow Micro-/Nanostructures. *Chem. Rev.* **2016**, *116*, 10983–11060.
- (74) Roca, M.; Haes, A. J. Silica-Void-Gold Nanoparticles : Temporally Stable Surface-Enhanced Raman Scattering Substrates. *J. Am. Chem. Soc.* **2008**, *130*, 14273–14279.
- (75) Watanabe, K.; Ishii, H.; Konno, M.; Imhof, A.; van Blaaderen, A.; Nagao, D. Yolk/Shell Colloidal Crystals Incorporating Movable Cores with Their Motion Controlled by an External Electric Field. *Langmuir* **2017**, *33*, 296–302.
- (76) Yao, Y.; Zhang, X.; Peng, J.; Yang, Q. One-Pot Fabrication of Yolk-Shell Nanospheres with Ultra-Small Au Nanoparticles for Catalysis. *Chem. Commun.* **2015**, *51*, 3750–3753.
- (77) Ding, H.; Zhang, Y.; Xu, S.; Li, G. A Wrinkle to Sub-100 nm Yolk/Shell Fe₃O₄@SiO₂ Nanoparticles. *Nano Res.* **2016**, *9*, 3632–3643.